

Ductile Fracture Prediction in Rotational Incremental Forming for Magnesium Alloy Sheets Using Combined Kinematic/Isotropic Hardening Model

DUC-TOAN NGUYEN, JIN-GEE PARK, and YOUNG-SUK KIM

To predict the ductile fracture of a magnesium alloy sheet when using rotational incremental forming, a combined kinematic and isotropic hardening law is implemented and evaluated from the histories of the ductile fracture value (I) using a finite element analysis. Here, the criterion for a ductile fracture, as developed by Oyane (*J. Mech. Work. Technol.*, 1980, vol. 4, pp. 65–81), is applied *via* a user material based on a finite element analysis. To simulate the effect of the large amount of heat generation at elements in the contact area due to the friction energy of the rotational tool-specimen interface on the equivalent stress-strain evolution in incremental forming, the Johnson-Cook (JC) model was applied and the results compared with equivalent stress-strain curves obtained from tensile tests at elevated temperatures. The finite element (FE) simulation results for a ductile fracture were compared with the experimental results for a (80 mm × 80 mm × 25 mm) square shape with a 45 and 60 deg wall angle, respectively, and a (80 mm × 80 mm × 20 mm) square shape with a 70 deg wall angle. The trends of the FE simulation results agreed quite well with the experimental results. Finally, the effects of the process parameters, *i.e.*, the tool down-step and tool radius, on the ductile fracture value and FLC at fracture (FLCF) were also investigated using the FE simulation results.

DOI: 10.1007/s11661-010-0235-1

© The Minerals, Metals & Materials Society and ASM International 2010

I. INTRODUCTION

AS the lightest structural alloys, magnesium alloys have many advantages compared with steel, cast iron, and even aluminum alloys.^[1] However, the structural use of magnesium alloys is seriously restricted by their limited ductility at room temperature (RT) due to their hexagonal-close-packed crystal structure.^[2,3]

Currently, the magnesium alloys used for automobile parts are mainly processed by die casting,^[4,5] which allows parts with complex geometry to be manufactured. Yet, the mechanical properties of such die cast parts invariably lack the required endurance strength and ductility.^[6] As an alternative, the required mechanical properties for magnesium alloys can be achieved using a forming process instead of die casting. Parts manufactured by forming can have a fine-grained structure without porosity and improved mechanical properties, such as endurance strength and ductility.^[7] Thus, research on mass-produced magnesium alloy sheets has increased.

To widen the application of Mg alloys, many studies have already investigated^[6–11] the sheet forming of magnesium alloys at elevated temperatures and reported that AZ31 sheets have a good stretchability and drawability at elevated temperatures between 423 K

(150 °C) and 573 K (300 °C). Therefore, the warm forming of AZ31 sheets within this temperature range is being further investigated from a practical point of view.

When Won *et al.*^[12] investigated the mechanical properties of magnesium alloys at elevated temperatures, they discovered that the Lankford value (R) for an AZ31 magnesium sheet decreases as the temperature increases; plus, the sheet becomes isotropic and recrystallizes above 473 K (200 °C). In addition, the studies by Won *et al.*^[12] and Choo *et al.*^[13] on the formability of magnesium alloy sheets at high temperatures revealed that a temperature over 473 K (200 °C) is required to achieve the safe forming of magnesium alloy sheets.

Incremental sheet forming (ISF) is an innovative process for manufacturing sheet metal products using CNC-controlled simple forming tool, which plastically deforms a blank according to the desired shape. The two main variations of ISF are positive and negative forming, referring to the side of the part that the tool works on. Thus, in negative forming, the tool works on the concave surface of the part, whereas in positive forming, the tool works on the convex surface. When investigating the forming limits for sheet materials when using ISF, Iseki and Kumon^[14] recorded much higher forming limit curves (FLCs) when compared to the FLCs based on theories of plastic instability. Thus, several studies have investigated the influence of the main material parameters and process variables on formability, and improve the formability in ISF.^[15–17] Kim and Yang^[18] proposed a double-forming technique to improve formability, assuming that only shear

DUC-TOAN NGUYEN and JIN-GEE PARK, Doctoral Candidates, and YOUNG-SUK KIM, Professor, are with the Department of Mechanical Engineering, Kyungpook National University, Daegu 702-701, Republic of Korea. Contact e-mail: caekim@knu.ac.kr

Manuscript submitted October 29, 2009.

Article published online May 18, 2010

deformation occurs in the material. Plus, Park *et al.*^[19] studied and showed the possibility of cup incremental forming of a magnesium sheet at RT with a rotational tool, where the tool rotates itself.

Nonetheless, even though ISF has been shown to improve the forming limits for aluminum and steel sheets when compared with press forming,^[14,20] the use of ISF for magnesium has received little attention, as magnesium is difficult to form at RT. Therefore, Park *et al.*^[19] proposed rotational incremental sheet forming, which improves the formability of sheet materials, when compared with ISF, due to the large amount of heat generated in the contact area as a result of the friction energy at the tool-specimen interface and plastic deformation energy from the shear deformation.

Accordingly, this study further investigates the use of rotational incremental forming for magnesium alloy sheets based on a finite element method (FEM) analysis. Fracture prediction using FEM is an easy and efficient way to apply a ductile fracture criterion and determine the influence of changed parameters. For this purpose, proper descriptions of the initial yield stress surface and its evolution, essential for the constitutive law in plasticity, must be considered. Normally, the isotropic hardening law overestimates the hardening component by missing the Bauschinger effect and transient behavior. Meanwhile, the kinematic hardening rule underestimates the hardening of a material and exaggerates the Bauschinger effect. Thus, a combined isotropic and kinematic hardening law is able to predict more accurately both the Bauschinger effect and the transient behavior. Furthermore, to apply a ductile fracture criterion, when Gouveia *et al.*^[20] examined the validity of four previously published fracture criteria, a generalized plastic work criterion and criteria developed by Cockcroft and Latham, Brozzo *et al.*, and Oyane, they found that Oyane's criterion is the best for use along with finite element results.

Therefore, in this study, the rotational incremental forming of a magnesium alloy sheet for various wall angles of a square shape is simulated using the ABAQUS/Explicit finite element code.^[21] Meanwhile, for the ductile failure criterion, Oyane's fracture criterion^[22] via a VUMAT subroutine based on a combined kinematic/isotropic hardening law and the Johnson–Cook (JC) model are used to predict fractures at elevated temperatures due to the movement of the rotational tool and friction energy at the tool-specimen interface. First, a combined kinematic/isotropic hardening law is applied for a uniaxial tension-compression test at RT to determine the scalar parameter β that makes the best fit for the stress-strain curves between the FE simulation and the experiment results for a magnesium alloy sheet. Next, the JC model is used to predict the stress-strain curves at elevated temperatures, which are then compared with the measured values. Finally, based on the relationship between the heat generation at the tool-specimen interface and the various wall angles, Oyane's fracture criterion is used to predict the fracture of magnesium alloy sheets when using rotational incremental forming. The effect of the process parameters on the ductile fracture value and FLC at fracture (FLCF) is also investigated.

II. MATERIAL AND HARDENING MODEL

A. Material

Table I shows the mechanical properties of the magnesium alloy sheet with a thickness of 1.0 mm. The parameters characterizing the uniaxial true stress-strain curve response of the material at RT used in the FE simulations are also given in the table in terms of the parameters in Swift's work-hardening law,^[23] using the following expression:

$$\bar{\sigma} = K \left(\varepsilon_0 + \varepsilon_{eq}^{pl} \right)^n \quad [1]$$

where K is the plastic coefficient; n is the work-hardening exponent; and $\bar{\sigma}$, ε_{eq}^{pl} , and ε_0 are the equivalent stress, equivalent strain, and yield strain, respectively.

Figure 1 shows the stress-strain curves obtained from the in-plane uniaxial compression and tension tests at RT. Figure 2 shows the experimental results for the yield loci, which were not symmetric, and the compressive behavior differed from the tensile behavior. These phenomena are unique to a magnesium alloy sheet and result from its crystal structure.

Table I. Mechanical Properties of Tested Material

Material	AZ31
Density (ρ , kg/mm ³)	1.77×10^{-6}
Young's modulus (E , kN/mm ²)	45,000
Poisson's ratio	0.35
Tension yield stress (σ_Y^T , MPa)	170
Compression yield stress (σ_Y^C , MPa)	100
Melting temperature (K (°C))	891 (618)
ε_0	0.0078
K (MPa)	406.8
n value	0.187

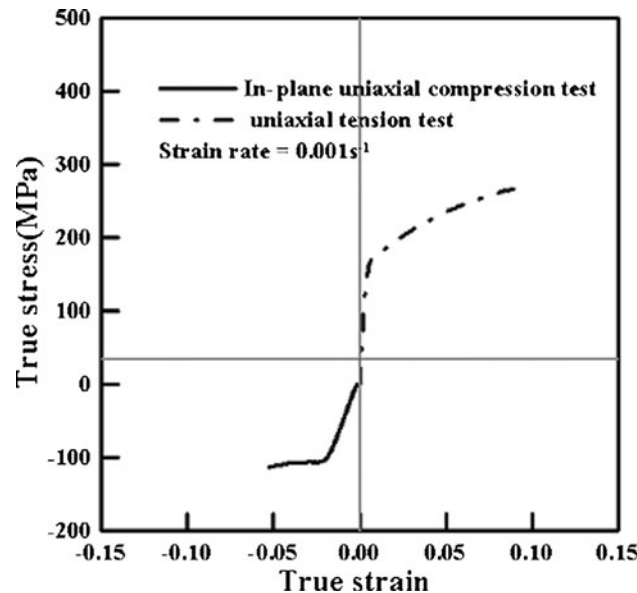


Fig. 1—Stress-strain curves obtained from in-plane uniaxial compression tests at RT (Ref. 19).

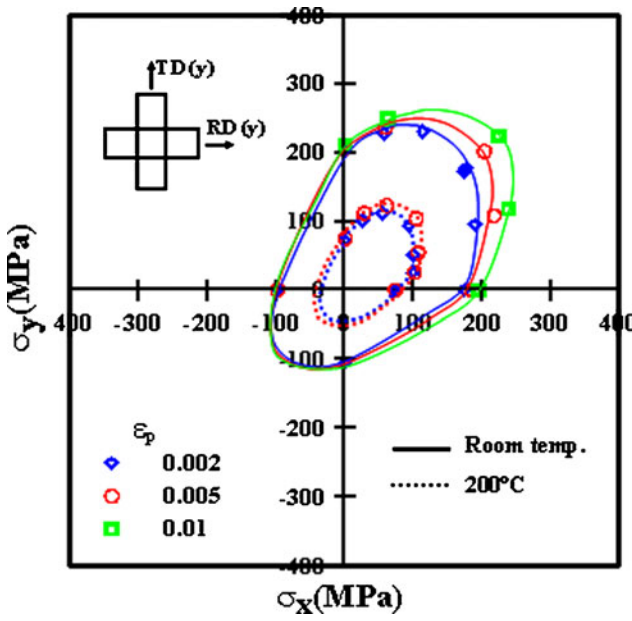


Fig. 2—Yield loci obtained from biaxial tensile tests and in-plane uniaxial compression tests (Ref. 19).

B. Hardening Models

1. Basic definitions

The Von Mises yield surface is defined as Eq. [2]:

$$f(\sigma) = \frac{1}{2} \xi_{ij} : \xi_{ij} - \frac{1}{3} \bar{\sigma}^2 \quad [2]$$

where $\bar{\sigma}$ is the uniaxial equivalent yield stress. The Von Mises yield surface is a cylinder in deviatoric stress space with a radius of Eq. [3]

$$R = \sqrt{\frac{2}{3}} \bar{\sigma} \quad [3]$$

If σ and σ_m are the current values of the stress and mean stress, respectively, the deviatoric part of the current stress is expressed as Eq. [4]:

$$S_{ij} = \sigma_{ij} - \sigma_m I \quad [4]$$

The stress difference, ξ , is the stress measured from the center of the yield surface, as shown in Eq. [5], where α is the back stress:

$$\xi_{ij} = S_{ij} - \alpha_{ij} \quad [5]$$

The normal to the Mises yield surface can be written as Eq. [6]:

$$Q_{ij} = \sqrt{\frac{3}{2}} \frac{\xi_{ij}}{\bar{\sigma}} \quad [6]$$

The plastic flow rule is calculated using Eq. [7]:

$$\dot{\varepsilon}_{ij}^{pl} = \gamma Q_{ij} \quad [7]$$

where γ is a scalar that must be determined and $\dot{\varepsilon}_{ij}^{pl}$ means the equivalent plastic strain.

2. Combined nonlinear hardening

The incremental forms of the governing equations are described subsequently.

The generalized Hooke's law is shown in Eq. [8]:

$$\Delta\sigma = \lambda \text{trace}(\Delta\varepsilon_{ij}^{el}) I + 2\mu \Delta\varepsilon_{ij}^{el} \quad [8]$$

The incremental analogs of the rate equation are shown by Eqs. [9] through [11]:

$$\sigma_{ij}|_{n+1} = \sigma_{ij}^{tr}|_{n+1} - 2\mu \Delta\gamma Q_{ij} \quad [9]$$

$$R|_{n+1} = R|_n + \frac{2}{3} \beta H \Delta\gamma \quad [10]$$

$$\alpha_{ij}|_{n+1} = \alpha_{ij}|_n + (1 - \beta) \frac{2}{3} \Delta\gamma H Q_{ij} \quad [11]$$

where H , the slope of the uniaxial yield stress vs the plastic strain curve, is calculated using Eq. [12], and β , the scalar parameter, is defined as ranging from 0 to 1. When $\beta = 0$, only kinematic hardening occurs, and when $\beta = 1$, only isotropic hardening occurs. Thus, for kinematic/isotropic hardening, β is determined by comparing the cyclic tensile curves between the experimental and simulation data.

$$H = \frac{d\bar{\sigma}}{d\varepsilon_{eq}^{pl}} = Kn \left(\varepsilon_0 + \varepsilon_{eq}^{pl} \right)^{n-1} \quad [12]$$

For the nonlinear kinematic/isotropic hardening model, the size of the yield surface was modified as a function of the equivalent plastic strain ε_{eq}^{pl} and possessed a relationship with the power law, as shown in Eq. [13]:

$$\bar{\sigma}_Y \left(\varepsilon_{eq}^{pl} \right) = \bar{\sigma} \left(\varepsilon_{eq}^{pl} \right) - H \varepsilon_{eq}^{pl} \quad [13]$$

During active plastic loading, the stress must remain on the yield surface, so that

$$\sqrt{Q_{ij} : Q_{ij}} = 1 \quad [14]$$

The equivalent plastic strain increment is related to $\Delta\gamma$ using Eq. [15]:

$$\Delta\varepsilon_{eq}^{pl} = \sqrt{\frac{2}{3}} \Delta\gamma \quad [15]$$

Taking the tensor product of this equation with Q , using the yield condition at the end of the increment, and solving for $\Delta\gamma$, as shown in Eq. [15],

$$\Delta\gamma = \frac{1}{2\mu \left(1 + \frac{H}{3\mu} \right)} \left(\left(\xi_{ij}^{\text{trial}}|_{n+1} : \xi_{ij}^{\text{trial}}|_{n+1} \right)^{1/2} - R_n \right) \quad [16]$$

III. FINITE ELEMENT PROCEDURES

In the FEM simulation, due to the asymmetric yield surface, the uniaxial true stress-strain curve response of

the material for the uniaxial compression test was assumed as Eq. [17]:

$$\bar{\sigma}^C = \frac{\sigma_Y^C}{\sigma_Y^T} K \left(\varepsilon_0 + \dot{\varepsilon}_{eq}^{pl} \right)^n \quad [17]$$

where K is the plastic coefficient; σ_Y^T and σ_Y^C are the tension and compression yield stresses; n is the work-hardening exponent; and $\bar{\sigma}^C$, $\dot{\varepsilon}_{eq}^{pl}$, and ε_0 are the equivalent stress in the compression zone, equivalent strain, and yield strain, respectively, as mentioned in Table I.

In this article, due to the low average R value (Lankford value) at an elevated temperature ($R \sim 1$ at 473 K (200 °C)), the Von Mises model was applied to the calculation.

A. Uniaxial Tension-Compression Test at RT

The aforementioned constitutive model was used with a commercial finite element program ABAQUS/Explicit via a VUMAT subroutine for the uniaxial tension-compression tests of standard ASTM tensile specimens with a rectangular cross section of 13-mm width and 1.0-mm thickness and a gage length of 50 mm in order to determine the scalar parameter β at RT. Here, the uniaxial tension-compression testing specimen was modeled using solid elements C3D8R, where the average element size of the solid elements was about 1 mm in width, 1 mm in length, and 0.33 mm in height. The stress-strain curves, obtained by the FE simulation via a VUMAT subroutine by changing the values of β , were compared with the stress-strain experimental data obtained from the uniaxial tension-compression test and the best fit chosen, as shown in Figure 3. The scalar

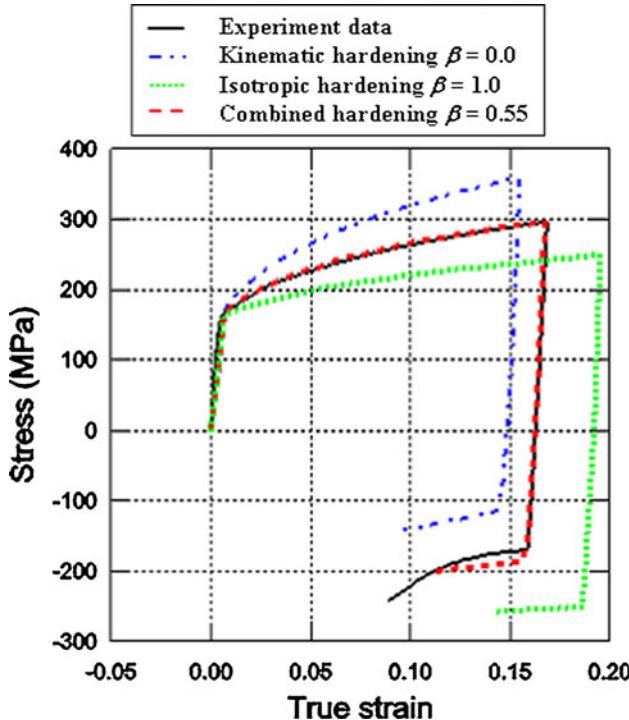


Fig. 3—Estimation of scalar parameter (β) from uniaxial tension-compression test simulation at RT.

parameter β for the combined kinematic/isotropic hardening was chosen as 0.55.

B. JC Model at Elevated Temperatures

The inelastic behavior of the investigated alloy was assumed to be described by the JC model,^[24] which is well suited to describe the mechanical behavior of materials at high strain rates and various temperatures. The JC model is generally used in an adiabatic transient dynamic analysis and is purely empirical, giving the following relation for the flow stress:

$$\bar{\sigma} = \left(A + B \left(\dot{\varepsilon}_{eq}^{pl} \right)^n \right) \left(1 + C \log \left(\frac{\dot{\varepsilon}_{eq}^{pl}}{\dot{\varepsilon}_0} \right) \right) \left(1 - \hat{T}^m \right) \quad [18]$$

where

$$\hat{T} = \begin{cases} 0 & \text{for } T < T_r \\ \frac{T - T_r}{T_m - T_r} & \text{for } T_r \leq T \leq T_m \\ 1 & \text{for } T > T_m \end{cases} \quad [19]$$

The terms A , B , C , n , and m are the material parameters to be identified; T is the current temperature; T_m is the melting temperature; and T_r is a reference temperature, i.e., 297 K (24 °C).

In this study, the unusual plastic behavior of a magnesium sheet was verified at elevated temperatures with a constant strain rate. In addition, the stress-strain curve was fitted, as in Eq. [1], allowing Eq. [18] to be expressed in the following reduced form:

$$\bar{\sigma} = K \left(\varepsilon_0 + \dot{\varepsilon}_{eq}^{pl} \right)^n \left(1 - \left(\frac{T - T_r}{T_m - T_r} \right)^m \right) \quad [20]$$

To determine m , quasi-static experimental results at both room and higher temperatures are needed. If quasi-static experiments, at the same strain rate, are carried out at two different temperatures, denoted by the superscripts in Eqs. [18] and [19], the ratio r between the stresses at a specific plastic strain can be expressed as

$$r = \frac{\bar{\sigma}^{(1)} \left(\dot{\varepsilon}_{eq}^{pl} \right)}{\bar{\sigma}^{(2)} \left(\dot{\varepsilon}_{eq}^{pl} \right)} = \frac{1 - \left(\hat{T}^{(1)} \right)^m}{1 - \left(\hat{T}^{(2)} \right)^m} \quad [21]$$

If $T^{(2)} = T_r$, then from Eq. [19], $\hat{T}^{(2)} = 0$ and m is given by

$$m = \frac{\log(1 - r)}{\log(\hat{T}^{(1)})} \quad [22]$$

The stresses shown in Figure 4 for temperatures of 373 K (100 °C), 423 K (150 °C), and 473 K (200 °C) were divided by the stresses at 297 K (24 °C) (RT) according to Eq. [21]. The results were the average values within the range of $0.05 < \dot{\varepsilon}_{eq}^{pl} < 0.25$, and were $r = 0.879$, $r = 0.712$, and $r = 0.444$ for 373 K (100 °C), 423 K (150 °C), and 473 K (200 °C), respectively. Substituting these values into Eq. [22] then resulted in $m = 1.027$ for 373 K (100 °C), $m = 0.802$

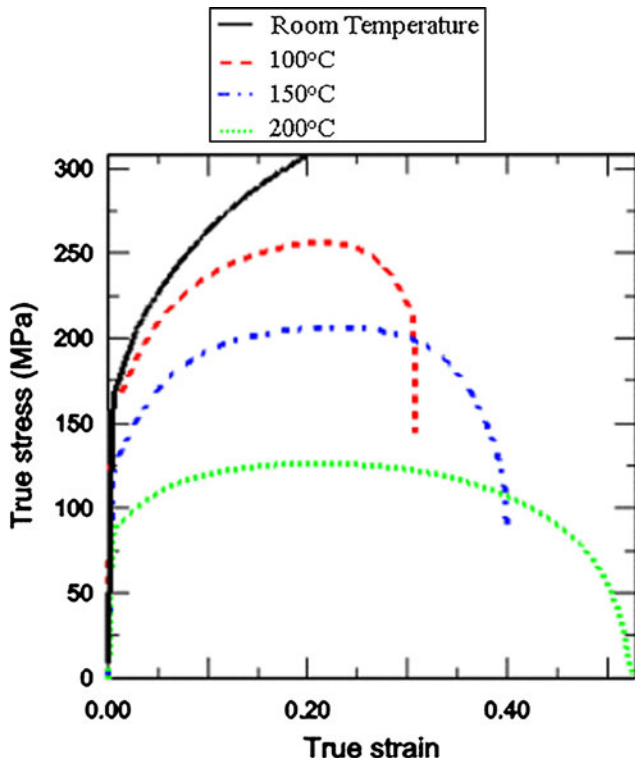


Fig. 4—Stress-strain curves based on measured values (Ref. 19).

for 423 K (150 °C), and $m = 0.48$ for 473 K (200 °C). Thus, an average value of $m = 0.77$ was adopted.

When adopting the JC model, Eq. [20] was used instead of Eq. [1] in the VUMAT subroutine for the tensile test simulation at 373 K (100 °C), 423 K (150 °C), and 473 K (200 °C). The FE simulation results are shown in Figure 5.

C. Problem Description, Geometry, and FE Models for Rotational Incremental Forming of Magnesium Alloy Sheet

The aforementioned model was applied for the square-shape rotational incremental forming of a magnesium alloy sheet, where the specimens were 150 mm (width) by 150 mm (length) by 1 mm (thickness). Meanwhile, the experimental model of the square shape was 80 mm (width) by 80 mm (length) by 25 mm (height). The depth increment was 0.4 mm in the z direction, and the wall angles of the square cup shape were determined as 45, 60, and 70 deg, respectively. The tool radius was 6 mm and the feed rate was 400 mm/min. As used in a previous study,^[19] in the experiment, the spindle speed of the tool was 4000 rpm counter-clockwise in the $-z$ direction until the temperature of the tool reached 373 K (100 °C) in the case of a 45 deg wall angle, and then set to 3000 rpm. When the temperature of the tool exceeded 373 K (100 °C), chips of magnesium were generated in the contact area between the specimen and the tool. Therefore, in the case of a 45 deg wall angle, 373 K (100 °C) was the maximum temperature without chip generating. Similarly, the maximum temperature was measured for the other wall angles, and

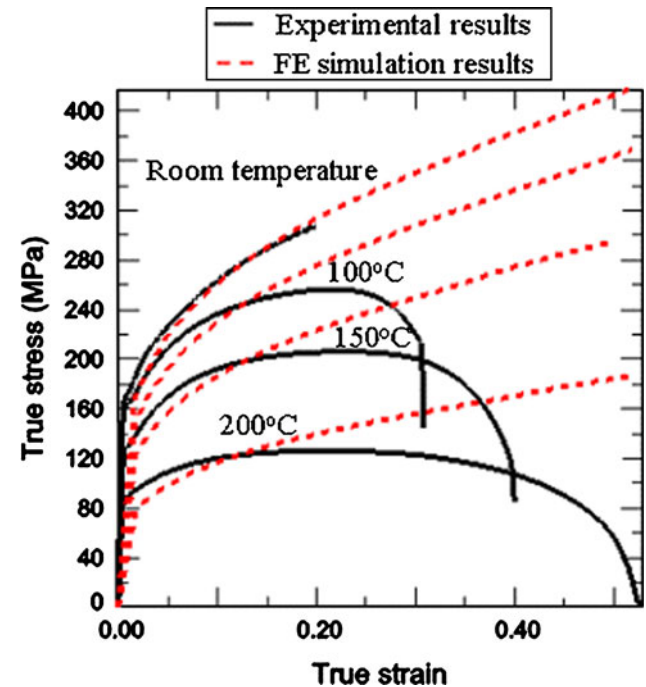


Fig. 5—Stress-strain curves based on FE simulation and comparison with measured values.

Table II. Maximum Temperature of the Tool and Specimen for Each Square Cup (Reference 19)

Wall Angle, θ (Deg)	Temperature of Tool (K (°C))	Temperature of Specimen (K (°C))
45	378 (105)	373 (100)
60	398 (125)	391 (118)
70	423 (150)	414 (141)

Table II shows the maximum temperature for the tool and specimen for each square cup.

As in previous experiments,^[19] no fractures were observed with a 45 deg wall angle, whereas fractures were observed with a 70 deg wall angle (Figure 6). The minor and major strains of a through e in Figure 6(c) were measured and are shown in Figure 8. Here, the open symbols (\triangle , \square , and \circ) represent the strain with a 45, 60, and 70 deg wall angle, respectively, and no fractures. Otherwise, the cross symbol (\times) represents the occurrence of a fracture in the wall and corner areas with a 70 deg wall angle.

As mentioned in previous literature,^[14,20] most of the FLCs in ISF (FLCF) appear to be a straight line with a negative slope in the positive region of the minor strain. Thus, when adopting this linear model (Figure 7) to formulate a FLC (FLCF), it can be expressed as follows:

$$\varepsilon_1 + 0.639\varepsilon_2 = 1.02 \quad [23]$$

Figure 8 shows the finite-element model used for the ISF test process. To simulate the experiments, only one quarter of the specimen was modeled, the blank was modeled using solid elements C3D8R, the punch was modeled using analytical rigid surface elements, and the die was modeled using rigid surface elements R3D4.

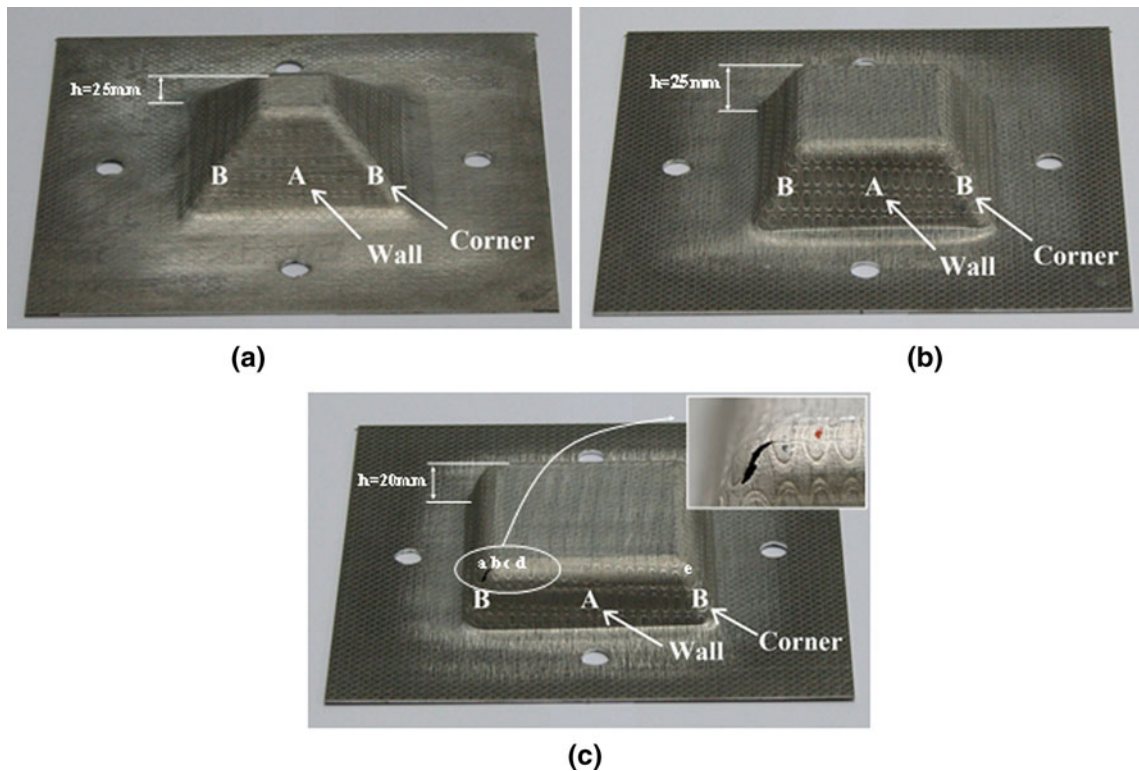


Fig. 6—Square cups formed by rotational ISF: (a) 45 deg wall angle, (b) 60 deg wall angle, and (c) 70 deg wall angle at which point cracks occurred (Ref. 19).

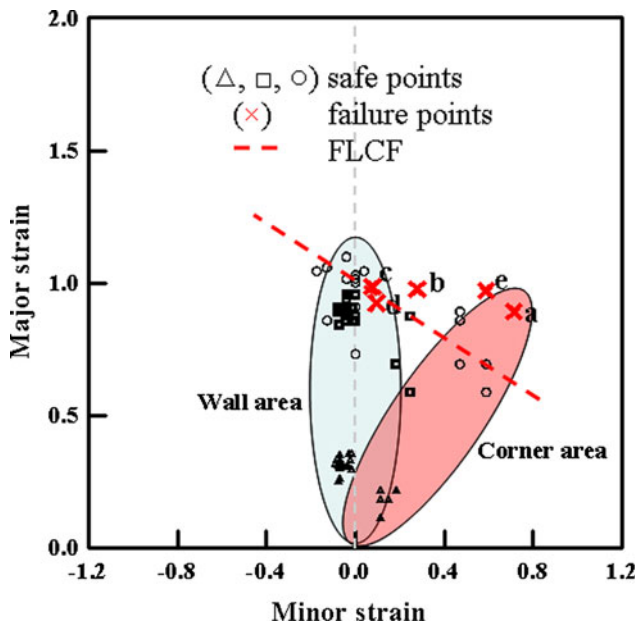


Fig. 7—Forming limit for rotational incremental forming.

Throughout this study, the average element size of the blank was about 1 mm in width, 1 mm in length, and 0.33 in thickness; the average element size of the rigid die was about 2 mm in width and 2 mm in length. While the die was fixed in all directions, the tool was allowed to move following the tool path and rotate involving the z direction at the center point of the tool. The friction

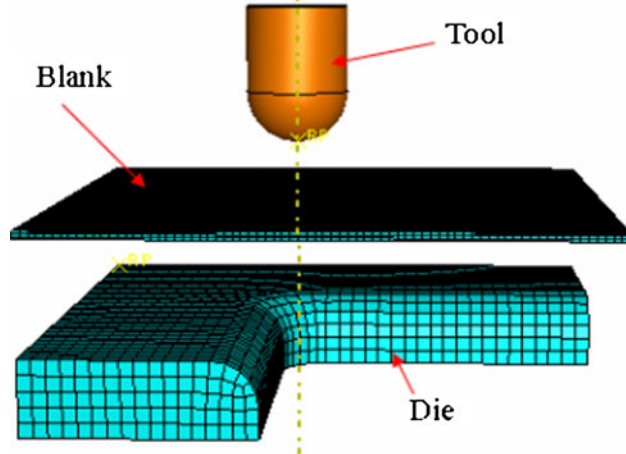


Fig. 8—Finite element model for incremental forming simulation.

behavior was modeled using the Coulomb friction law. The friction coefficient μ_1 between the blank and the punch was assumed to be the same as the friction coefficient μ_2 between the blank and a die of 0.1. The other physical properties of the materials used in the analysis are shown in Table III.

D. Ductile Fracture Criterion

Based on various hypotheses, several criteria have already been proposed for ductile fractures.^[26,27] Oyane *et al.*^[22] proposed a criterion allowing for the history of

Table III. Thermophysical Properties of Magnesium Alloy AZ31 as a Function of Temperature T (in °C) (Reference 25)

Thermophysical Property	AZ31
Thermal conductivity (W/(m K))	$77 + 0.096 T$
Specific heat capacity (J/(kg K))	$1000 + 0.666 T$
Thermal coefficient expansion (K^{-1})	2.48×10^5

the hydrostatic stress affecting the occurrence of a ductile fracture, and this has been widely applied in the field of bulk forming with a high reliability.^[22,27] This criterion has also been used by Takuda *et al.*^[28] to predict fracture initiation for the deep drawing processes of laminated composite sheets. However, while the results have been successful for fracture prediction, it should be mentioned that the application of a ductile fracture criterion is more effective for low ductility materials. Thus, in the present study, the criterion of Oyane *et al.*^[22] was employed, as in Eq. [24]:

$$\int_0^{\bar{\varepsilon}_f} \left(\frac{\sigma_m}{\bar{\sigma}} + C_1 \right) d\bar{\varepsilon} = C_2 \quad [24]$$

At a uniaxial tension, Eq. [24] can be expressed as follows:

$$\left(\frac{1}{3} + C_1 \right) \varepsilon_{1f(\text{tensile})} = C_2 \quad [25]$$

while at a plane strain tension, Eq. [24] can be written as Eq. [26]:

$$\left(\frac{2}{3} + \frac{2}{\sqrt{3}} C_1 \right) \varepsilon_{1f(\text{plane-strain})} = C_2 \quad [26]$$

where $\bar{\varepsilon}_f$ and ε_{1f} are the equivalent strain and major strain, respectively, at which a fracture occurs; σ_m is the hydrostatic stress; $\bar{\sigma}$ is the equivalent stress; $\bar{\varepsilon}$ is the equivalent strain; and C_1 and C_2 are the material constants.

To determine the material constants C_1 and C_2 in Eq. [24], destructive tests have to be operated under at least two types of stress condition. Here, using the FLCF in Eq. [23], the fracture strains for a uniaxial tension ($\varepsilon_{1f(\text{tensile})}$) and plane strain tension ($\varepsilon_{1f(\text{plane-strain})}$) were calculated as 1.499 and 1.02, respectively. From this result, the material constants C_1 and C_2 for the ductile fracture criterion were calculated following Eqs. [25] and [26] as 0.563 and 1.344, respectively.

Oyane's ductile criterion in Eq. [24] was combined with the proposed hardening model and JC model, and then coded into a VUMAT subroutine.

When rewriting the criterion for a ductile fracture in Eq. [24], the following integral was obtained:

$$I = \frac{1}{C_2} \int_0^{\bar{\varepsilon}_f} \left(\frac{\sigma_m}{\bar{\sigma}} + C_1 \right) d\bar{\varepsilon} \quad [27]$$

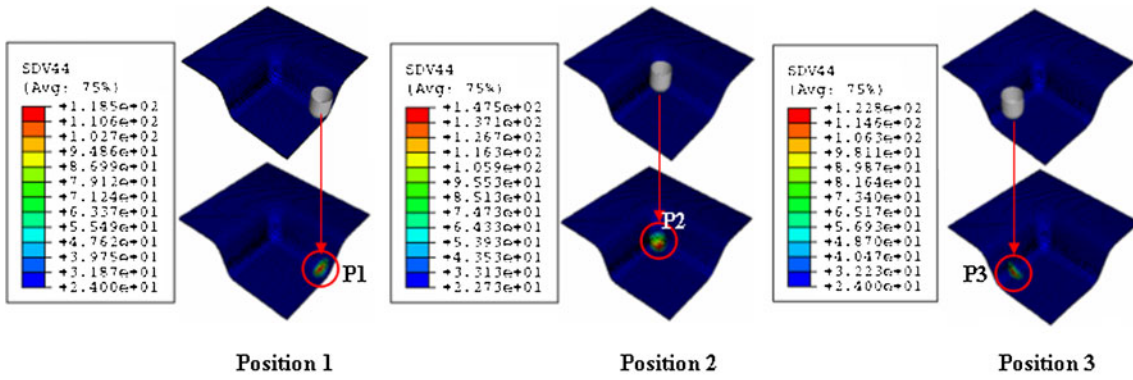
The histories of stress and strain in each element during forming were calculated using the FEM, and the ductile

fracture integral I in Eq. [27] was obtained for each element. When the integral value I in Eq. [27] reaches 1.0, a fracture will occur. Therefore, this ductile fracture value I was calculated for every finite element during the forming process.

IV. RESULTS AND DISCUSSION

Figure 9(a) shows the FE simulation results of the heat generation (SDV44) in the contact area between the specimen and the tool for three different tool positions, while Figure 9(b) depicts the evolution of the temperature at the elements corresponding to the three tool positions in Figure 9(a) for the case of a 70 deg wall angle. The results show that the maximum temperatures in the FE simulation of 420 K (147 °C) at the corners and about 395 K (122 °C) in the wall areas were in good agreement with the experimental measurement of 414 K (141 °C) given in Table II. To verify the effect of the heat generation on the stress-strain curve without considering the JC model, an equivalent stress-strain evolution in incremental forming at a deformed element, obtained by an FE simulation *via* a VUMAT subroutine, was compared with other stress-strain curves at elevated temperatures obtained when adopting the JC model for the tensile test simulation in Figure 5, as shown in Figure 10(a). Although the FE simulation effectively predicted the heat generation, the boundary profile of the equivalent stress-strain evolution in incremental forming without considering the JC model still followed the stress-strain curve at RT. Thus, in this study, the heat generation at the elements in the contact area between the specimen and the tool was calculated when considering the JC model using Eq. [20] and coded into a VUMAT subroutine for the incremental forming simulation. The equivalent stress-strain evolution in this case is shown in Figure 10(b). The boundary profile of the equivalent stress-strain evolution, which was limited by the stress-strain curves at RT and 423 K (150 °C) in the tensile test simulation, proved the effect of the heat generation on the stress-strain curve, thereby showing its suitability for tensile tests at elevated temperatures. Therefore, this method can be applied to predict ductile fractures in FE simulations of the rotational incremental forming of magnesium alloys.

The FE simulation results for three test cases with an equivalent plastic strain $\bar{\varepsilon}$ (SDV7) and the maximum ductile fracture value I (SDV9) calculated from Eq. [27] *via* a VUMAT subroutine based on a combined kinematic/isotropic hardening law are presented in Figure 11. The simulation results showed that the maximum values of the fracture ductile integral I for the (80 mm × 80 mm × 25 mm) square shape with 40 and 60 deg wall angles, corresponding to a maximum temperature of 378 K (105 °C) and 399 K (126 °C), were 0.513 and 0.898, respectively, *i.e.*, smaller than 1.00. This means that no failure occurred in these cases. Meanwhile, in the case of the (80 mm × 80 mm × 20 mm) square shape with a 70 deg wall angle, corresponding to a maximum temperature of 420 K (147 °C), the FE simulation results gave a maximum value for the ductile

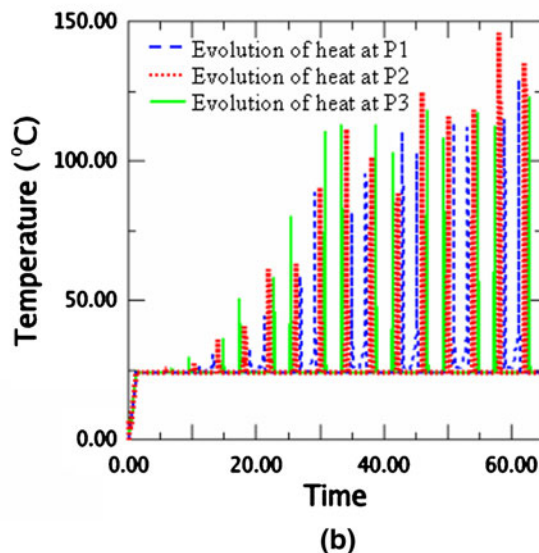


Position 1

Position 2

Position 3

(a)



(b)

Fig. 9—Heat generation in contact areas between specimen and tool.

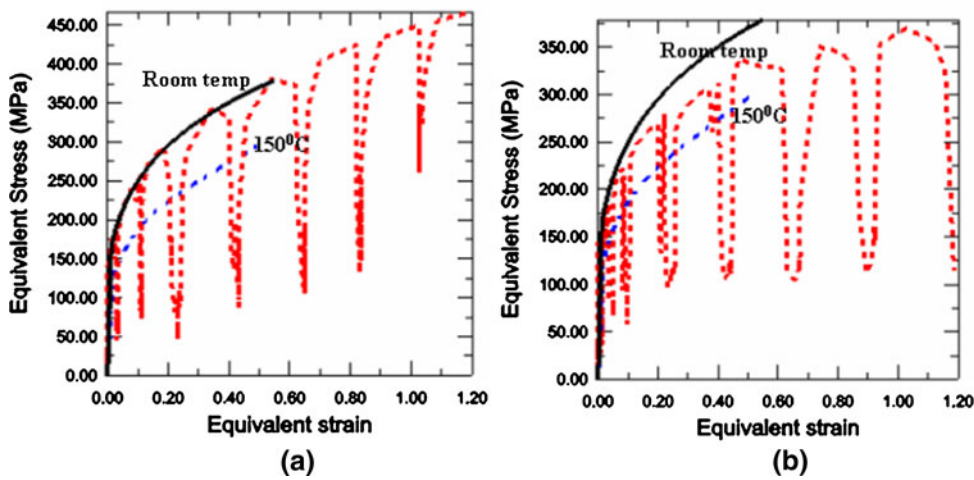


Fig. 10—Evolution of equivalent stress-strain curve for incremental forming: (a) without considering JC model and (b) when considering JC model.

fracture integral I equal to 1.242 and failure appeared. The trends of the failure sites predicted in this study also agreed well with those in the actual experiments.

After the simulation, it was concluded that to obtain a sound final product, the wall angle of the square shape needed to be smaller than 70 deg. Plus, even

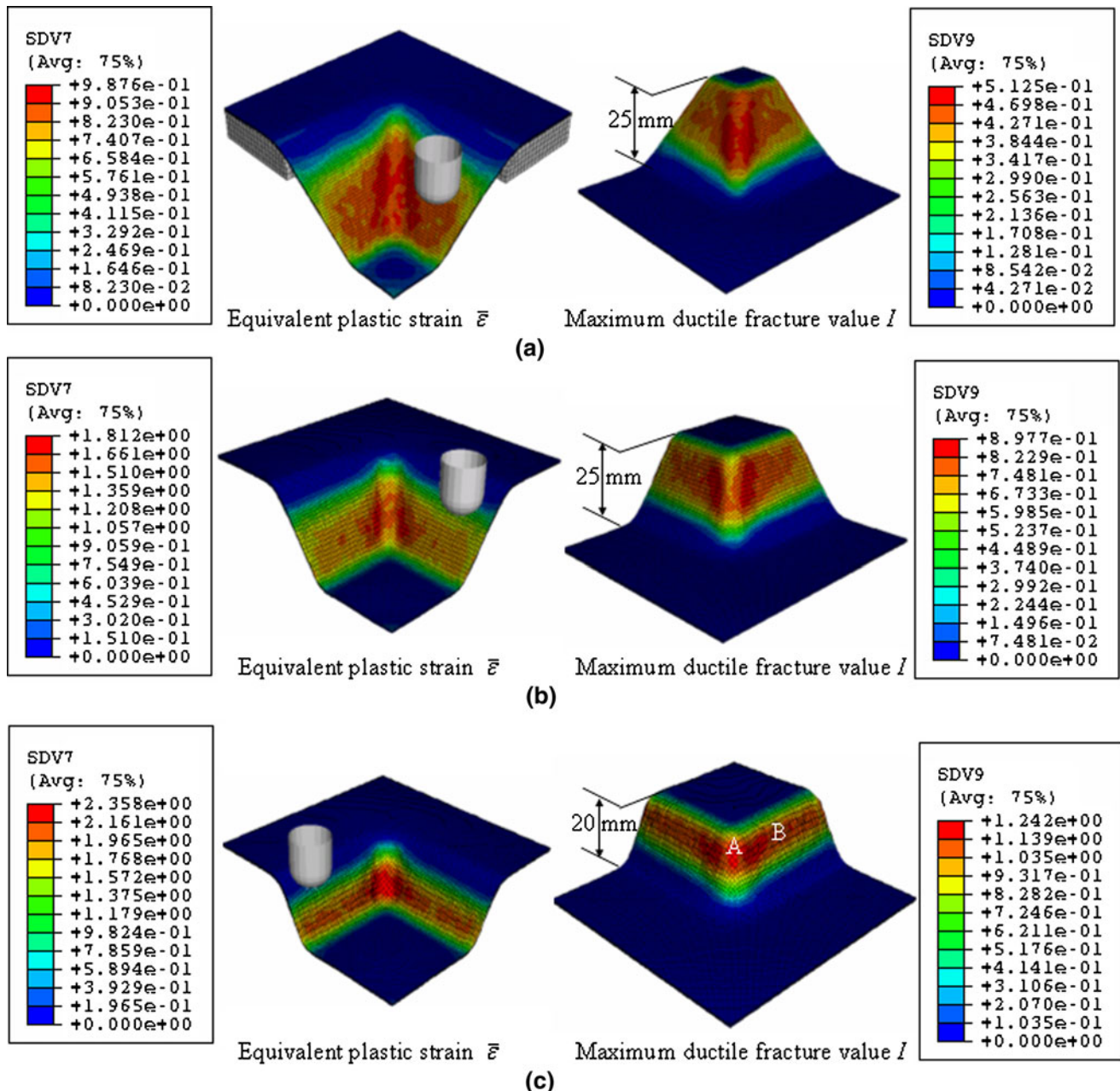


Fig. 11—Deformed shape in finite element simulation: (a) 45 deg wall angle, (b) 60 deg wall angle, and (c) 70 deg wall angle.

though the heat generation was smaller than that in the case of the 70 deg wall angle, the 45 and 60 deg wall angles were deformed to the final shape without any failure.

To predict the FLCF using the FE simulation results, a new method was used, as shown in Figure 12. Figure 12(a) shows the evolutional strain paths at the element of the corner area (point A in Figure 11(c)) and the element of the wall area (point B in Figure 11(c)). These strain paths are suitable for the paths of equal biaxial stretching and plane strain. Figure 12(b) presents the evolutions of the ductile fracture integral I at the elements of the concerned points (A and B) vs the major strain. From Figure 12(b), the major strains at the

occurrence of a fracture ($I = 1$) at the concerned points of equal biaxial stretching and plane strain were determined as 0.665 and 1.017, respectively. Figure 12(c) depicts the FLCF obtained when adopting a linear model through the points where fractures occurred in the FE simulations. This FLCF agreed quite well with the previous assumptions of Eq. [23] and Figure 8.

A. Effect of Tool Down-Step

To verify the effect of a tool down-step (H), an analysis was carried out for a tool down-step (H) of 0.8 mm and 1.2 mm, and the results were then compared with those for $H = 0.4$ mm discussed earlier for

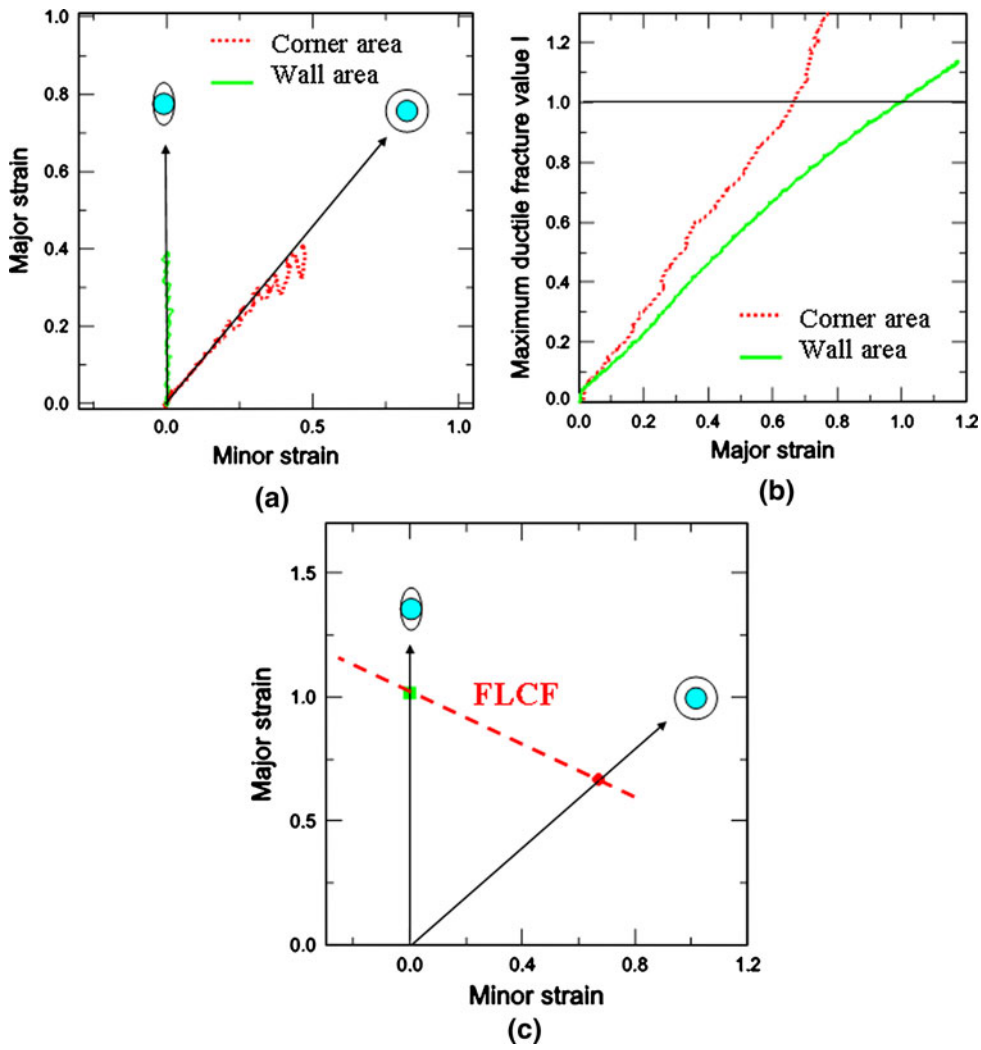


Fig. 12—FLCF obtained from FE simulation for corner and wall area with 70 deg wall angle.

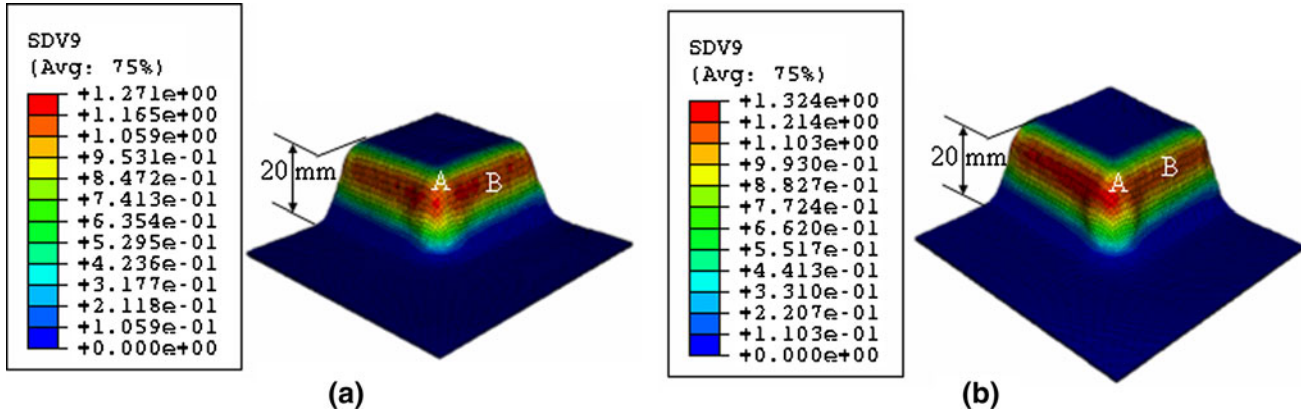


Fig. 13—Deformed shape in FE simulation with 70 deg wall angle, tool radius of 6 mm, and (a) tool down-step of 0.8 mm and (b) tool down-step of 1.2 mm.

the case of a (80 mm \times 80 mm \times 20 mm) square shape with a 70 deg wall angle corresponding to a temperature of 413 K (140 °C) and tool radius (R) of 6 mm. As shown in Figure 13, the maximum values of the ductile

fracture integral I in these cases were predicted to be 1.271 and 1.324, respectively. Thus, with a higher tool down-step, the maximum values of the ductile fracture integral I were higher, due to the larger deformation.

Figure 14 presents the FLCF obtained when adopting a linear model through the fracture points ($I = 1$) of equal biaxial stretching and plane strain for all three cases. When the down-step increased from 0.4 to 0.8 mm and 1.2 mm, the major fracture strains of equal biaxial stretching and plane strain decreased to 0.613 and 0.544, and 0.94 and 0.85, respectively, so that the FLCF moved down, making it clear that the formability became lower as the down-step increased. These results were similar to the experimental results and conclusions of a previous study.^[16]

B. Effect of Tool Radius

The effect of the tool radius (R) was investigated based on an analysis of the following two cases: $R = 4$ and 8 mm. The analysis was carried out for the case of a (80 mm \times 80 mm \times 20 mm) square shape with a 70 deg wall angle and tool down-step (H) of 0.4 mm.

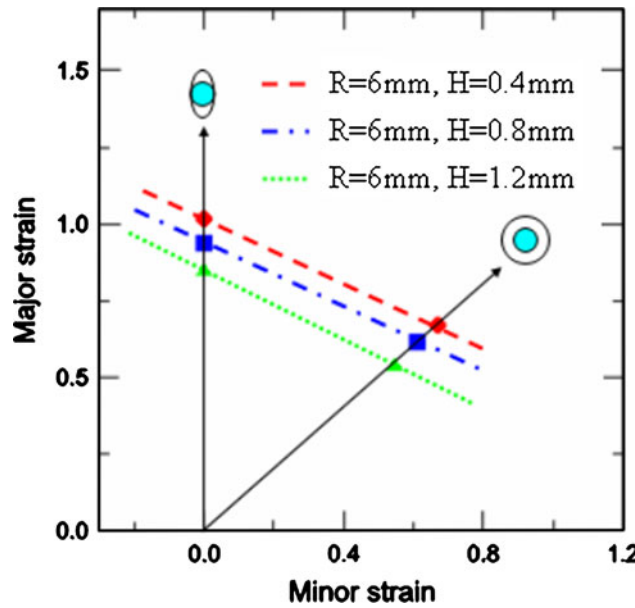


Fig. 14—FLCF with different tool down-steps and 6-mm tool radius.

The maximum values of the ductile fracture integral I were found to be 1.229 and 1.258, respectively, as shown in Figure 15. Figure 16 depicts the FLCF when the tool radius changed from 6 to 4 mm and 8 mm. The FLCF was lower in the case of the 8-mm tool radius with the major fracture strains of equal biaxial stretching and plane strain at 0.614 and 0.927, respectively. Meanwhile, in the case of the 4-mm tool radius, the major fracture strain increased to 0.717 for the equal biaxial stretching and decreased to 0.597 in the plane strain area. Thus, as the tool radius increased, the deformation zone or contact zone increased and the level of strain decreased, resulting in incremental formability.

V. CONCLUSIONS

To predict the fracture of a magnesium alloy sheet when using rotational incremental forming, the heat

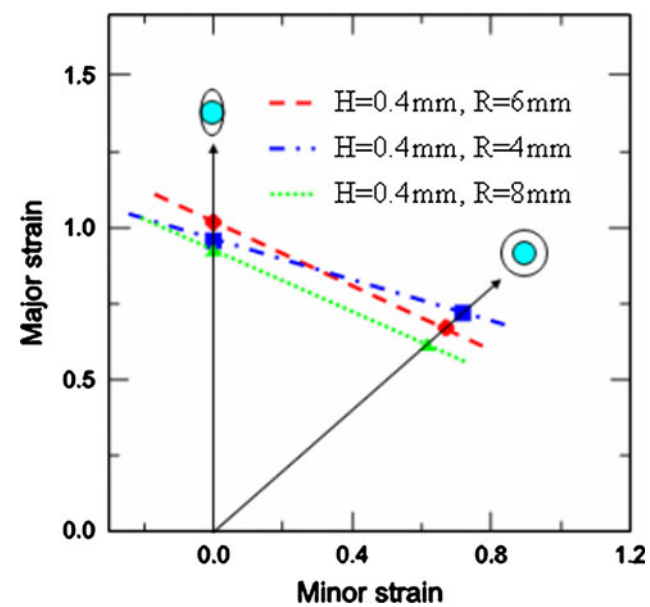


Fig. 16—FLCF with different tool radii and 0.4-mm tool down-step.

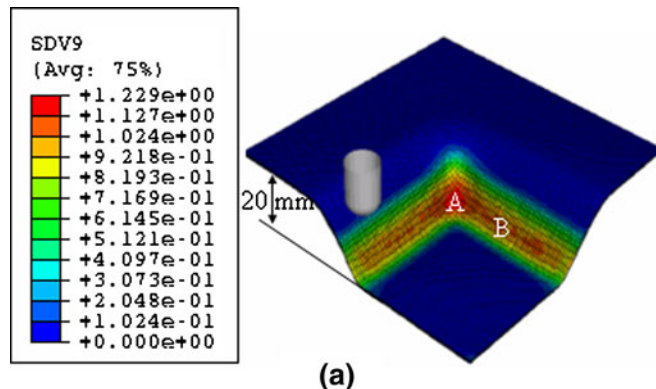
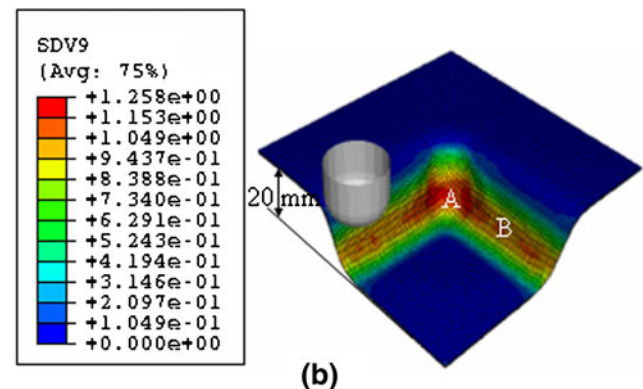


Fig. 15—Deformed shape in FE simulation with 70 deg wall angle, tool down-step of 0.8 mm, and (a) tool radius of 4 mm and (b) tool radius of 8 mm.



generation at the elements resulting from the rotational tool and contact area between the specimen and the tool was investigated using finite element simulations and the Johnson–Cook model, and the estimates were then compared with experimental results for a square shape with 45, 60, and 70 deg wall angles. Commercial software (ABAQUS version 6.5, explicit formulation) with a user-defined subroutine (VUMAT) based on a combined kinematic/isotropic hardening model was used for the simulation. The FE simulation results showed that when the wall angles of a (80 mm × 80 mm × 25 mm) square shape were smaller than 60 deg, the maximum value for the fracture ductile integral I was less than 1, meaning no fracture would occur. The predicted failure sites matched well with the experimental results. The FLCF prediction and effect of the process parameters on the FLCF FE simulation results showed that the formability decreased as the tool down-step or tool radius increased, which agrees well with previous conclusions^[16] on ISF.

ACKNOWLEDGMENTS

The authors gratefully acknowledge the financial support from the Brain Korea 21 project at Kyungpook National University sponsored by the Korean Ministry of Education, Science and Technology. This work was also partially supported by a grant from the Korean Ministry of Education, Science and Technology, The Regional Core Research Program/Medical Convergence Technology Development Consortium for Anti-aging and Well-being.

REFERENCES

1. R.S. Busk: *Magnesium Production Design*, Marcel Dekker Inc., New York, NY, 1986, p. 13.
2. E. Aghion, B. Bronfin, and D. Eliezer: *J. Mater. Process. Technol.*, 2001, vol. 117, pp. 381–85.
3. M.T. Perez-Prado and O.A. Ruano: *Scripta Mater.*, 2002, vol. 46, pp. 149–55.
4. N.A. El-Mahallawy, M.A. Taha, E. Pokora, and F. Klein: *J. Mater. Process. Technol.*, 1998, vol. 73, pp. 125–38.
5. B.H. Hu, K.K. Tong, X.P. Niu, and I. Pinwill: *J. Mater. Process. Technol.*, 2000, vol. 105, pp. 128–33.
6. E. Doege and K. Droder: *J. Mater. Process. Technol.*, 2001, vol. 115, pp. 14–19.
7. H. Friedrich and S. Schumann: *J. Mater. Process. Technol.*, 2001, vol. 117, pp. 276–81.
8. H. Takuda, T. Enami, K. Kubota, and N. Hatta: *J. Mater. Process. Technol.*, 2000, vol. 101, pp. 281–86.
9. S. Lee, Y.H. Chen, and J.Y. Wang: *J. Mater. Process. Technol.*, 2002, vol. 124, pp. 19–24.
10. E. Doege and K. Droder: *J. Mater. Process. Technol.*, 1997, vols. 7–8, pp. 19–23.
11. M. Kohzu, F. Yoshida, and H. Somekawa: *Mater. Trans.*, 2001, vol. 42, pp. 1273–76.
12. S.W. Won, S.G. Oh, K. Osakada, J.G. Park, and Y.S. Kim: *2004 Proc. Spring Conf. Kor. Soc. Technol. Plasticity*, 2004, pp. 53–56.
13. D.K. Choo, S.W. Oh, J.H. Lee, and C.G. Kang: *Trans. Mater. Process.*, 2005, vol. 14, pp. 628–34.
14. H. Iseki and H. Kumon: *J. Jpn. Soc. Technol. Plasticity*, 1994, vol. 35 (406), pp. 1336–41.
15. L. Fratini, G. Ambrogio, R. Di Lorenzo, L. Filice, and F. Micari: *Ann. CIRP*, 2004, vol. 53 (1), pp. 207–10.
16. Y.H. Kim and J.J. Park: *J. Mater. Process. Technol.*, 2002, vols. 130–131, pp. 42–46.
17. G. Ambrogio, I. Costantino, L. De Napoli, L. Filice, L. Fratini, and M. Muzzupappa: *J. Mater. Process. Technol.*, 2004, vols. 153C–154C, pp. 501–07.
18. T.J. Kim and D.Y. Yang: *Int. J. Mech. Sci.*, 2000, vol. 42, pp. 1271–86.
19. J.G. Park, J.H. Kim, N.K. Park, and Y.S. Kim: *Metall. Mater. Trans. A.*, 2010, vol. 41A, pp. 97–105.
20. B.P.P.A. Gouveia, J.M.C. Rodrigues, and P.A.F. Martins: *Int. J. Mech. Sci.*, 1996, vol. 38, pp. 361–72.
21. D. Hibbit, B. Karlsson, and P. Sorensen: *ABAQUS User's Manual*, Ver. 6.5.1. Abaqus Inc., Pawtucket, RI, 2003.
22. M. Oyane, T. Sato, K. Okimoto, and S. Shima: *J. Mech. Work. Technol.*, 1980, vol. 4, pp. 65–81.
23. H.W. Swift: *J. Mech. Phys. Solids.*, 1952, vol. 1, pp. 1–18.
24. G.J. Johnson and W.H. Cook: *Proc. 7th Int. Symp. on Ballistics*, The Hague, 1983, pp. 541–47.
25. S.G. Hibbins: in *Light Metals 1998 Metaux Legers*, M. Sahoo and C.C. Fradet, eds., TMS-CIM, Calgary, AB, Canada, 1998, pp. 265–80.
26. S.E. Clift, P. Hartley, C.E.N. Sturgess, and G.W. Rowe: *Int. J. Mech. Sci.*, 1990, vol. 32, pp. 1–17.
27. M. Toda, T. Miki, S. Yanagimoto, and K. Osakada: *J. Jpn. Soc. Technol. Plasticity*, 1988, vol. 29, pp. 971–76.
28. H. Takuda, K. Mori, H. Fujimoto, and N. Hatta: *J. Mater. Process. Technol.*, 1996, vol. 60, pp. 291–96.